

Energy correction based on fluorescence attenuation of DAMPE

Libo Wu^{1,2}, Yunlong Zhang^{1,2}, Zhiyong Zhang^{1,2}, Yifeng Wei^{1,2}, Sicheng Wen^{1,2}, Haoting Dai^{1,2}, Chengming Liu^{1,2}, Xiaolian Wang^{1,2}, Zizong Xu^{1,2} and Guangshun Huang^{1,2}

¹ State Key Laboratory of Particle Detection and Electronics, University of Science and Technology of China, Hefei, Anhui 230026, China; zhzhy@ustc.edu.cn, weiyf@ustc.edu.cn

² Department of Modern Physics, University of Science and Technology of China, Hefei, Anhui 230026, China

Received 20xx month day; accepted 20xx month day

Abstract The major scientific goals of DArk Matter Particle Explorer (DAMPE) are to study cosmic-ray electrons (including positrons) and gamma rays from 5 GeV to 10 TeV and nuclei from $Z = 1$ to 26 up to 100 TeV. The deposited energy measured by the Bismuth Germanate Oxide (BGO) calorimeter of DAMPE is affected by fluorescence attenuation in BGO crystals that are 600 mm long. In this work, an in-orbit attenuation calibration method is reported, and energy correction of the sensitive detector unit of the BGO calorimeter is also presented.

Key words: DAMPE, BGO calorimeter, Fluorescence attenuation, Dark Matter

1 INTRODUCTION

The DArk Matter Particle Explorer (DAMPE) ([Chang et al. 2017](#); [Ambrosi et al. 2017, 2019](#); [Yuan & Feng 2018](#)), a satellite-borne experiment funded by the Chinese Academy of Sciences, was launched into a sun-synchronous orbit at an altitude of 500 km in December 2015 from the Jiuquan Satellite Launch Center. The scientific objectives of DAMPE include searching for the signature of dark matter particles ([Gianfranco et al. 2005](#); [Lu et al. 2014](#)), understanding the mechanisms of particle acceleration operating in astrophysical sources ([An et al. 2019](#)), and studying gamma-ray emission from Galactic and extragalactic sources ([Duan et al. 2019](#); [Xu et al. 2018](#)).

DAMPE, as shown in Fig. 1, consists of four sub-detectors. From top to bottom, they are the Plastic Scintillator Detector (PSD) ([Ding et al. 2019](#); [Ma et al. 2014](#)), Silicon–Tungsten tracKer (STK) ([Azzarello et al. 2016](#)), Bismuth Germanium Oxide (BGO) calorimeter ([Wu et al. 2018](#); [Zhang et al. 2015, 2019](#)), and NeUtron Detector (NUD) ([He et al. 2016](#)). The PSD, which is composed of two orthogonal layers of plastic scintillator strips with dimensions of $884 \times 28 \times 10$ mm, is designed to measure the charge of incoming nuclei via the Z^2 dependence of the specific ionization loss in a double layer up to $Z = 26$, and it aids in

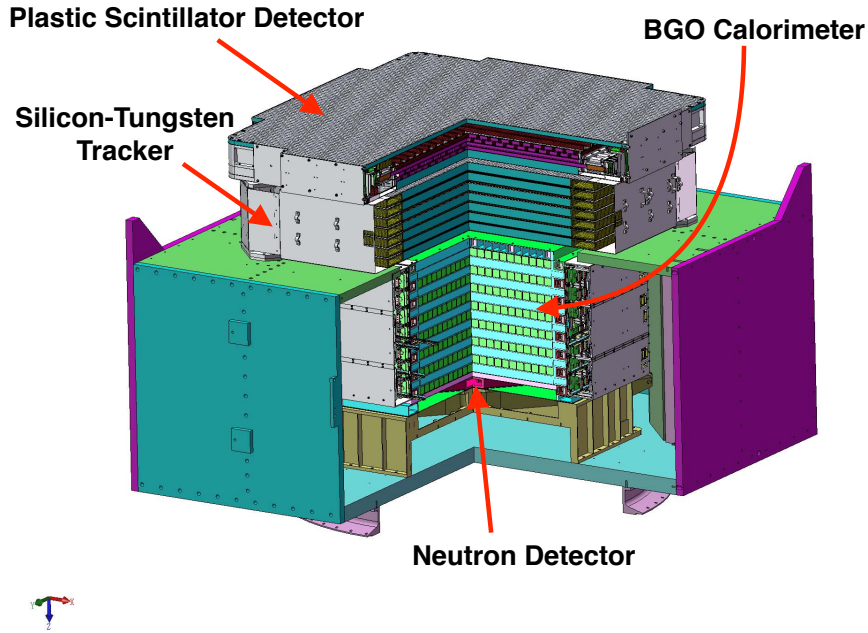


Fig. 1: Side view of the DAMPE detector.

of position-sensitive silicon microstrip detectors. Three layers of tungsten are inserted inside layers 2, 3, and 4 to convert gamma rays in electron–positron pairs. The STK enables reconstruction of the trajectory and charge of an event. The BGO calorimeter contains 14 layers with 31 radiation lengths and ~ 1.6 nuclear interaction lengths in total (Wei et al. 2016). Each layer has 22 BGO bars, which are arranged horizontally. The BGO bars of neighboring layers are arranged in an orthogonal way to measure the energy deposition and profile of hadron and electromagnetic showers developed in the BGO calorimeter. Moreover, the BGO provides the trigger for the whole DAMPE system. The NUD is composed of four boron-loaded plastic scintillators, each with a set of photomultiplier tubes (PMTs) and related electronics. It provides additional electron–hadron discrimination, which is important for energies above TeV.

Because of the thick BGO calorimeter (Wu et al. 2018), the energy range of DAMPE can cover from 5 GeV to 10 TeV for electrons and gamma rays and from tens of GeV to hundreds of TeV for cosmic protons and heavier nuclei. The BGO calorimeter is composed of 308 BGO crystal bars with dimensions $25 \times 25 \times 600$ mm (produced by the Shanghai Institute of Ceramics), which is the longest BGO crystal available at the time of development. The deposited energy in a BGO bar is independently measured by means of the fluorescent quantities collected by the PMTs at the two ends. The fluorescent photons transmitted along the BGO bar are unavoidably attenuated, so energy correction for this fluorescent attenuation must be taken into account.

2 ATTENUATION LENGTH CALIBRATION

Figure 2 shows a 600-mm-long BGO crystal bar (Ji et al. 2014). PMTs are connected to the BGO crystal at both ends (Side0 and Side1) (Zhang et al. 2015, 2012; Feng et al. 2015) to collect fluorescent lights, which is exponentially attenuated with the distance between the hit position and the PMT. Limited by



Fig. 2: BGO crystal with dimension of $25 \times 25 \times 600$ mm.

point marked by a red cycle in Fig. 2; When scintillating light pass through this region, the absorption and reflection efficiency of the spot to them is very different from other regions. This will cause the energy ratio of reconstruction at both ends to jump here, as shown in Fig. 4. In order to eliminate this effect, this paper developed a method to calibrate the attenuation lengths of the crystal at both sides of the spot respectively, and apply them to energy correction.

2.1 Method of calibration

By considering the energy resolution and the flux of incident particles, all cosmic-ray events are used to calibrate the scintillation attenuation length. The following event selection criteria should be applied:

- Energy requirement: The total energy deposited in the BGO calorimeter should be > 10 GeV.
- Track requirement: The BGO track should match the STK track to get an accurate position measurement of the track
- BarID match requirement: The BGO crystal hit by the track of each layer must have maximum energy deposition in the layer.
- Acceptance requirement: The events should be in the range of the acceptance angle of the DAMPE detector.

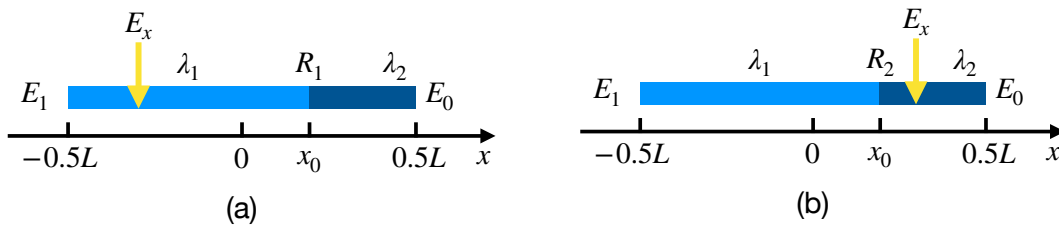


Fig. 3: Schematic plots of a BGO bar with its parameters of interest, showing (a) a hit position on the left side and (b) a hit position on the right side.

Figure 3 illustrates the true deposited energy E_x at hit position x , energies E_0 , E_1 measured from the side 0 and side 1, independently, and the cutoff point x_0 . The origin of the x axis is set at the middle of the BGO bar of total length $L = 600$ mm. λ_1 and λ_2 are the fluorescent attenuation lengths of the two parts ($-0.5L$ to x_0) and (x_0 to $0.5L$), respectively. There are two cases: Either the hit position is to the left (Fig. 3(a)) of the cutoff point or it is to the right (Fig. 3(b)); the calibration methods are similar. For the case of Fig. 3(a), following the law of fluorescent attenuation, the measured energies E_0 and E_1 , which are proportional to the fluorescent quantities collected by the PMTs of side 0 and 1, can be expressed as:

$$(x_0 - x) \quad (0.5L - x_0)$$

$$E_1 = E_x \times e^{-\frac{x+0.5L}{\lambda_1}} \quad (2)$$

where E_x is the true deposited energy at position x (from -300 to 300 mm) in the BGO bar and R_1 in formula (1) is the transparent coefficient when fluorescent photons pass through the cut point x_0 from the left to right.

The attenuation length of the left part ($x < x_0$) can be calibrated with the following function derived from functions (1) and (2):

$$\ln\left(\frac{E_0}{E_1}\right) = \frac{2x}{\lambda_1} + \left[\frac{0.5L - x_0}{\lambda_1} + \frac{x_0 - 0.5L}{\lambda_2} + \ln R_1\right] \quad (3)$$

Similarly, for the cases when particles are incident on the right ($x > x_0$), the attenuation length λ_2 can be calibrated by using formula (4), where R_2 is the transparent coefficient when fluorescent photons pass through the cutoff point x_0 from right to left.

$$\ln\left(\frac{E_0}{E_1}\right) = \frac{2x}{\lambda_2} + \left[\frac{0.5L + x_0}{\lambda_1} - \frac{0.5L + x_0}{\lambda_2} + \ln \frac{1}{R_2}\right] \quad (4)$$

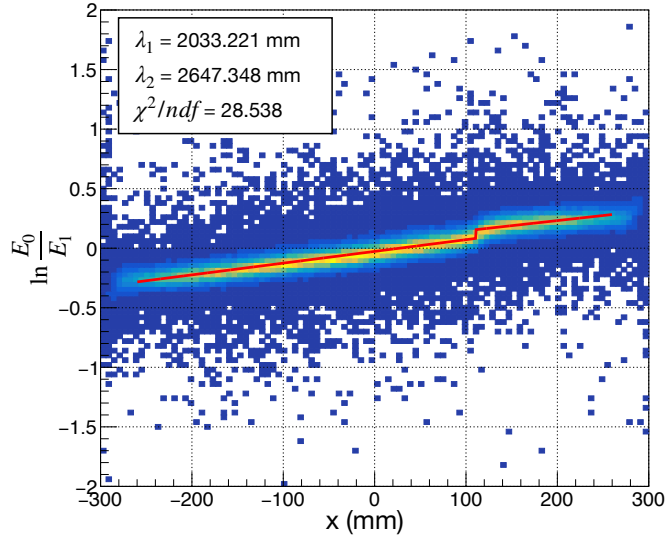


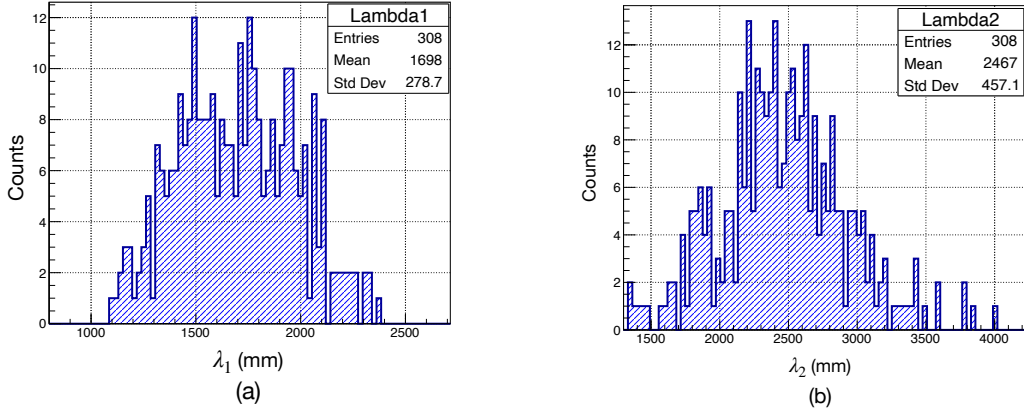
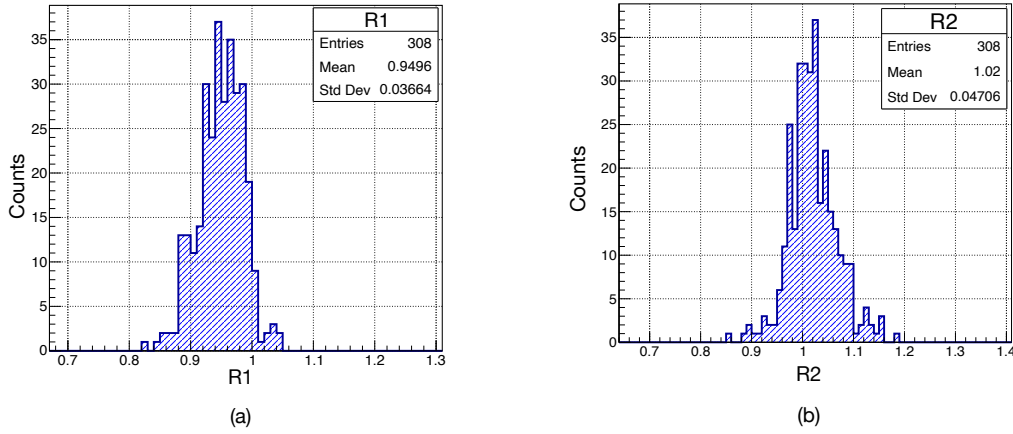
Fig. 4: Scatterplot of $\ln \frac{E_0}{E_1}$ versus hit position x . The fit range is from -260 mm to 260 mm.

Taking an example of the attenuation length calibration of a BGO bar (No. 10, layer 3), the hit position x and the measured energies E_0 and E_1 are, event by event, reconstructed according the event track fitting and ADC counts readout from electronics of the both sides. Fig.4 shows a typical scatterplot of $\ln \frac{E_0}{E_1}$ versus x of the BGO bar at No.10 of layer 3.

2.2 Calibration results

Fitting the scatterplot of Fig. 4 with the formulas (3) and (4) gives fluorescent attenuation lengths of the BGO bar of $\lambda_1 = 2033$ mm and $\lambda_2 = 2647$ mm. The parameters R_1 and R_2 can be calculated from the intercept of the fitting line. The same calibration program was applied to all 308 piece of the BGO bars. Figure 5 and 6 show the distributions of λ_1 and λ_2 and R_1 and R_2 , respectively, for the BGO calorimeter.

A database of the calibration parameters of the 308 pieces of the BGO bar (λ_1 , λ_2 and R_1 , R_2 , x_0) has

Fig. 5: Distributions of attenuation lengths of all BGO crystals: (a) λ_1 ; (b).Fig. 6: Distribution ratios of the variation of scintillation intensity. (a) R_1 ; (b) R_2 .

3 ENERGY CORRECTION BASED ON ATTENUATION LENGTH

In the experiment, the measured energies E_0 and E_1 are different from the true deposited energy at the hit position x because of the fluorescent attenuation, as shown in formulas (1) and (2). Therefore, it is necessary to perform an energy correction to account for fluorescence attenuation for each BGO crystal.

3.1 Method of energy correction

By using the database, the true deposited energy at hit position x can be, event by event, corrected for each BGO bar by means of the following formulas:

$$E_{x_0} = E_0 \times e^{\frac{x_0-x}{\lambda_1}} \times e^{\frac{0.5L-x_0}{\lambda_2}} \times \frac{1}{R_1} \quad (5)$$

$$E_{x_1} = E_1 \times e^{\frac{x+0.5L}{\lambda_1}} \quad (6)$$

$$E_{x_0} = E_0 \times e^{\frac{0.5L-x}{\lambda_2}} \quad (7)$$

$$E_{x_1} = E_1 \times e^{\frac{x-x_0}{\lambda_2}} \times e^{\frac{x_0+0.5L}{\lambda_1}} \times \frac{1}{R_2} \quad (8)$$

where formulas (5) and (6) are energy correction for cases when particles hit the left part ($x < x_0$) of

are the energies at side 0 and side 1 after the attenuation correction, respectively. Moreover, the hit position reconstructed by track of each layer is used to correct the energy of each BGO bars of the corresponding layer.

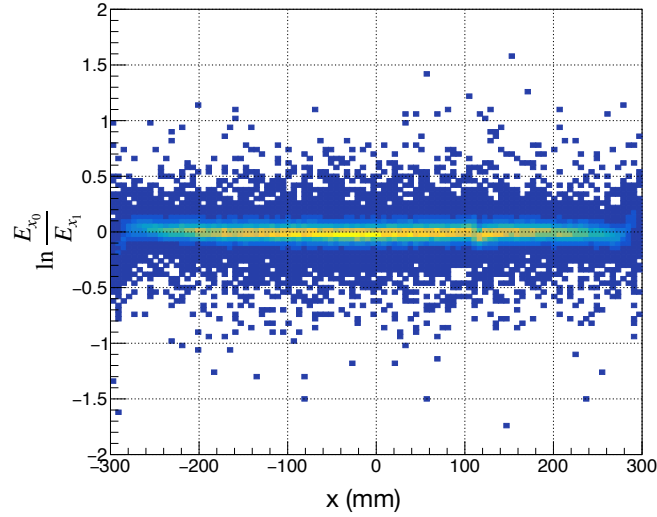


Fig. 7: Scatterplot of $\ln \frac{E_{x_0}}{E_{x_1}}$ versus hit position of x after energy correction.

3.2 Energy correction results

The correlation between $\ln \frac{E_0}{E_1}$ and hit position (x) of the BGO bar (No. 10, layer 3) after correction is shown in Fig. 7. Note that the distribution is flatter than that in Fig. 4, without a jump at x_0 . Figure 8 shows a comparison of the relationship of the energies at the two sides before (Fig. 8(a)) and after (Fig. 8(b)) correction. The plot in Fig. 8(b) demonstrates that, after energy correction, E_{x_0} and E_{x_1} measured at the two sides are getting closer to each other and become two independent measures of the true deposited energy at hit position x . Therefore, the correction program will increase the energy measurement accuracy and redundancy.

The total deposited energy can be obtained by using the correction method on all BGO crystals, and the distributions of the ratio of total deposited energy at the two sides before and after correction are shown in Figs. 9(a) and 9(b), respectively. The peak value is 0.998 after correction, which is more closer to 1 than the result before correction, and the standard deviation after correction is 0.046, which is much less than the result of 0.141 before correction.

4 CONCLUSION

There really is fluorescence attenuation in BGO crystal, which will influence the energy reconstructed at both sides. An in-orbit method to calibrate attenuation length based on the unique BGO crystals of DAMPE has been studied, and a database of calibration parameters has been set up. Upon completion of the energy correction for fluorescence attenuation, the consistency between energy measurements at the two sides was

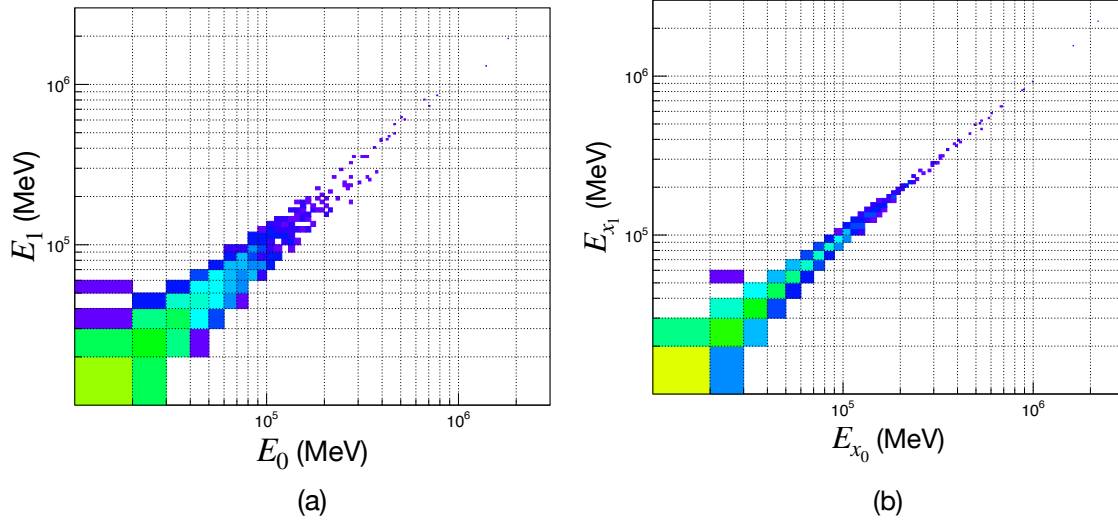


Fig. 8: Comparison of the relationships of the energies at the two sides (a) before correction and (b) after correction.

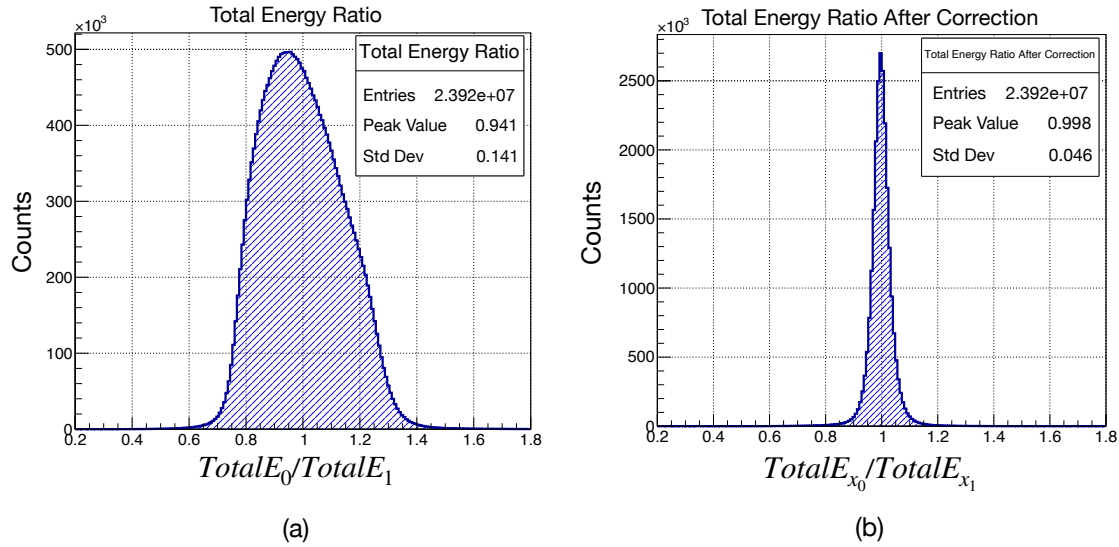


Fig. 9: Ratios of the total deposited energies reconstructed from the side 0 and side 1 of all BGO crystals: (a) before correction; (b) after correction.

energy E_x , and the energy resolution and redundancy capability of the BGO calorimeter were significantly improved.

Acknowledgements This work is supported by the Project supported by the Joint Funds of the National Natural Science Foundation of China (No. U1738135, U1738208 and U1738139), the National Natural Science Foundation of China (No. 11673021 and No. 11705197) and the National Key Research and Development Program of China (2016YFA0400200 and 2016YFA0400202).

References

Ambrosi, G., An, Q., Asfandiyarov, R., et al. 2017, Nature, 552(7683): 63.

- Azzarello, P., Ambrosi, G., Asfandiyarov, R., et al. 2016, Nuclear Instruments and Methods in Physics Research Section A, 831, 378-384.
- An, Q., Asfandiyarov, R., et al. 2019, Science Advances, 5(9): eaax3793.
- Chang, J., Ambrosi, G., An, Q., et al. 2017, Astroparticle Physics, 95: 6-24
- Duan, K.-K., Jiang, W., et al. 2019, Research in Astronomy and Astrophysics, 19(9): 122
- Ding, M., Zhang, Y.-P., Zhang, Y.-J., et al. 2019, Research in Astronomy and Astrophysics, 19(3): 047
- Feng, C.-Q., Zhang, D., et al., 2015, IEEE Transactions on Nuclear Science, 62(6): 3117-3125.
- Gianfranco, B., Dan, H. et al. 2005, Physics reports, 405(5-6): 279-390.
- He, M., Ma, T., Chang, J., et al. 2016, Chinese Astronomy and Astrophysics, 40(4): 474-482.
- Ji, Z., Ni, H., Yuan, L., et al. 2014, Nuclear Instruments and Methods in Physics Research Section A, 753: 143-148
- Lu, T.-S., Dong, T.-K., et al. 2014, Research in Astronomy and Astrophysics, 14(5): 520.
- Ma, P.-X., Zhang, Y.-J., Zhang, Y.-P., et al. 2019, Research in Astronomy and Astrophysics, 19(6): 082.
- Wu, L.-B., Wen, S.-C., Liu, C.-M., et al. 2018, IEEE Transactions on Nuclear Science, 65(8): 2007-2012
- Wei, Y.-F., Zhang, Z.-Y., Zhang, Y.-L., et al. 2016, IEEE Transactions on Nuclear Science, 63(2): 548-551.
- Xu, Z.-L., Duan, K.-K., et al. 2018, Research in Astronomy and Astrophysics, 18(3): 027.
- Yuan, Q. & Feng, L. 2018, SCIENCE CHINA Physics, Mechanics & Astronomy, 61(10): 101002.
- Zhang, Y.-Q., Guo, J.-H., et al. 2019, Research in Astronomy and Astrophysics, 19(9): 123.
- Zhang, Y.-L., Li, B., Feng, C.-Q., et al. 2012, Chinese physics C, 36(1): 71.
- Zhang, Z.-Y., Zhang, Y.-L., Dong, J.-N., et al. 2015, Nuclear Instruments and Methods in Physics Research Section A, 780: 21-26